Crystal Surfaces and Fate of Photogenerated Defects in Shape Controlled Anatase Nanocrystals: Drawing Useful Relations to Improve the H_2 Yield in Methanol Photosteam Reforming

Massimiliano D'Arienzo[*1], Maria Vittoria Dozzi*[*2], Matteo Redaelli [1], Barbara Di Credico[1], Franca Morazzoni[1], Roberto Scotti[1], Stefano Polizzi[3]*

[1]INSTM, Department of Materials Science, University of Milano-Bicocca, Via R. Cozzi 55, I-20125 Milano, Italy.

[2] Dipartimento di Chimica, Università degli Studi di Milano, Via Golgi 19, 20133 Milano, Italy

[3] Department of Molecular Sciences and Nanosystems, University Ca' Foscari of Venezia, Via Torino 155/b, I-30172 Venezia-Mestre, Italy

KEYWORDS: TiO_2, crystal faces, H_2 production, ESR Spectroscopy

ABSTRACT

In the present study, we comprehensively explored the photocatalytic properties, in H_2 production by methanol photosteam reforming, of anatase nanocrystals with nearly rectangular- (*RC*), rhombic- (*R*) and nanobar- (*NB*) shapes, having exposed {001}, {101} and {010} surfaces. The aim was to relate the reactivity both to the type of crystal faces and to the photogenerated defects.

The ESR spectra reveal that the amount of Ti^{3+} (electrons traps) is parallel to the H_2 evolution rate and becomes maximum for the *RC* nanocrystals which display the highest area of {001} surfaces and the lowest of {101} ones, but also involve a significant area of {010} faces. This points out that the H_2 production cannot be related only to the envisaged reducing {101} facets, but that the {010} ones play a key role.

We suggest that the contiguous {001}, {101} and {010} facets form an highly effective "surface heterojunction" within a *RC* nanoparticle, which drives the electrons photogenerated on {001} faces not just toward the {101} but also to the {010} ones, while the holes toward the {001} ones. This transfer improves the charge separation, thus boosting the photoefficiency of *RC* nanocrystals compared to that of *NB* and *R* ones.

The ESR spectra performed after UV excitation in the presence of MeOH show the partial annihilation of the Ti^{3+} features, mainly for highly reactive *RC* nanocrystals. Since H_2 production involves an electron transfer to the proton, a relevant role in H^+ photoreduction of the Ti^{3+} centers present on the exposed {010} and {101} surfaces is suggested.

These findings underline the importance to draw relations between the photogenerated defects and the exposed crystal surfaces, in order to optimize the photocatalytic properties of anatase nanocrystals.

INTRODUCTION

The production of hydrogen by photocatalytic water splitting or by photoreforming of sustainable organics (e.g. methanol, ethanol, and glycerol) can be envisaged as an ideal solution to face the current energy and environmental issues.[1-7]Among the photocatalysts potentially suitable for this purpose,[8-11] titanium dioxide (TiO_2) is by far the most widely used and numerous studies have been made in order to enhance its activity in H_2 photoproduction.[5-7,12-17] In general, TiO_2 efficiency can be improved (i) by doping TiO_2 with different elements (e.g., metals[13,14], p-block elements[15]); (ii) by modifying its surface with cocatalysts;[13-15] (iii) by mixing TiO_2 with another semiconductor oxide (i.e. metal-oxide heterojunctions);[16] (iv) by controlling the crystal phase, size, shape and surface properties of TiO_2 nanocrystals.[5,17] All these modifications aim both at favoring the separation of photogenerated charges and at harvesting visible light, thus enhancing the catalysts performance.

In recent years, significant attention has been devoted to the design of titania nanostructures characterized by tailored morphology and highly reactive exposed crystal surfaces.[17-20] In fact, the arrangement and coordination of the surface atoms on the different crystal facets have been proved to significantly affect the photoactivity of TiO_2 nanocrystals.[18-27] For instance, it has been suggested that the high reactivity of the anatase {001} face in the dissociative water adsorption

can be related to the high density of undercoordinated Ti^{3+} centers and to the presence of enlarged Ti–O–Ti bond angles at the surface, which make titanium and oxygen centers very reactive.[21,22] These properties inspired the use of {001}-faceted TiO_2 nanocrystals in many photocatalytic applications, namely for hydrogen production.[21-26] Recent results suggest that the presence of a high percentage of exposed {001} surfaces is not the only prerequisite to obtain high H_2 evolution rates. In fact, Liu et al. reported that microcrystals with predominant {001} facets provide less abundant H_2 evolution than crystals with predominantly exposed {101} surfaces.[27] Furthermore, the highest H_2 amount is associated to particles where the {001} surfaces are present together with a high percentage of {010} facets.

In this complex scenario it appears mandatory a further in-depth investigation on the relations between the nanocrystal face structure and the fate of photogenerated charge carriers, holes and electrons, involved in this photocatalytic reaction.

Recently, some of us reported that different crystal facets in anatase shape-controlled nanoparticles favor the stability of charge trapping centers (Ti^{3+}, O^-, and O_2^-) with consequent enhancement of the photocatalytic performance.[18] In particular, the detection of these paramagnetic defects by electron spin resonance spectroscopy indicated that the {001} facets play a major role in the photocatalytic process by providing oxidation sites, while the {101} facets, which provide reductive sites, indirectly contribute to the photoxidative processes.[18]

Along this direction, in the present study the surface properties of three differently shaped anatase nanocrystals, having specific exposed {001}, {101} and {010} crystal surfaces, are

associated to the photogenerated defects and, in turn, to their efficiency in photocatalytic hydrogen production.

In detail, nearly rectangular- (*RC*), rhombic- (*R*) and nanobar- (*NB*) shaped TiO_2 nanoparticles have been prepared by a previously reported solvothermal synthesis[28] using different ratios of titania precursor (titanium butoxide) and specific capping agents (oleic acid and oleylamine). After complete removal of the residual capping agents from the surface, the photocatalytic efficiency in hydrogen production by methanol (MeOH) photo steam reforming has been evaluated.

The reaction performance has been related to the exposed surfaces as well as to the amount and reactivity of the charge trapping centers (Ti^{3+}, O^- and O_2^-) detected by electron spin resonance (ESR) spectroscopy.

The results suggested a charge carrier transfer among {001}, {101} and {010} surfaces, which inhibits charge recombination and enhance the yield of H_2 evolution.

EXPERIMENTAL SECTION

Chemicals. Titanium(IV) butoxide ($Ti(OBu)_4$ or TB, 97%), oleic acid ($C_{18}H_{33}CO_2H$ or OA, 90%), oleylamine ($C_{18}H_{35}NH_2$ or OM, 70%) and the superhydride solution (1 M lithium triethylborohydride, $LiEt_3BH$ in THF) were all purchased from Aldrich and used without further purification.

Synthesis of shape-controlled TiO_2 nanocrystals. The solvothermal synthesis of shape controlled anatase nanocrystals was performed according to a previously reported procedure,[28]

by reaction of the titanium butoxide precursor (TB) in the presence of oleic acid (OA) and oleyl amine (OM). By simply changing the TB/OA/OM molar ratios and the reaction temperature, anatase nanocrystals with well-defined morphology were obtained.

In a typical experiment TB (22 mmol or 44 mmol) was added to different OA and OM mixtures in 25 mL absolute ethanol. The TB/OA/OM molar ratios were varied in order to obtain nearly rectangular- (*RC*, TB/OA/OM = 2:5:5), rhombic- (*R*, TB/OA/OM = 1:4:6), and small nanobar- (*NB*, TB/OA/OM = 1:8:2) shaped nanocrystals. For example, to synthesize rhombic shaped TiO_2 (*R*), 22 mmol of TB were added to a mixture containing 88 mmol of OA, 132 mmol of OM in 25 mL of absolute ethanol. The obtained mixture was stirred for 15 min and then transferred into a 400 mL Teflon-lined stainless steel autoclave containing 85 mL of absolute ethanol and 3.5 mL of Milli-Q water. The system was then heated to 140 °C or 180 °C and kept at this temperature for 18 h. After decantation, the TiO_2 powder was recovered from the autoclave, washed with ethanol several times, filtered and finally dried in vacuo ($p < 10^{-2}$ mbar) at room temperature. Hereafter, TiO_2 nanoparticles with rectangular, rhombic and nanobar shapes are labeled as *RC*, *R* and *NB*, respectively.

Morphological characterization. Transmission electron microscopy (TEM), High resolution TEM (HRTEM) images and selected area electron diffraction (SAED) patterns were obtained by using a Jeol 3010 apparatus operating at 300 kV with a high-resolution pole piece (0.17 nm point-to-point resolution) and equipped with a Gatan slow-scan 794 CCD camera. Samples were prepared by placing 5 μL drop of a dilute toluene dispersion of the nanocrystals on a holey carbon film supported on a 3 mm copper grid.

The percentage of exposed {101} and {001} faces for *R* and *NB* nanocrystals were calculated by the geometrical model developed by Jaroniec et al.[29] A similar model was utilized to determine the percentage of {010} facets in *RC* nanocrystals, by means of equation (1):

$$\%S\{010\} = \frac{S\{010\}}{S\{001\}+S\{010\}+S\{101\}} = \frac{2bc}{2a^2+2bc+\frac{b^2-a^2}{cos\,(68.3°)}} \quad (1)$$

where 68.3° is the angle between the {101} and the {001} faces, *a* and *b* correspond to the minimum and the maximum sides of the square {001} face in anatase and *c* is the longer side of the {010} rectangular surface (Figure 1). The percentage of the other exposed facets was also determined by geometrical models analogous to that leading to equation (1).

The average *a*, *b*, and *c* values were evaluated by measuring the size of ~ 100 particles in TEM images.

Nitrogen physisorption measurements were carried out with a Quantachrome Autosorb-1 apparatus. The specific surface area (SSA_{BET}, BET method[30]) and pore size distribution (BJH method[31]) were determined after evacuation at 200 °C for 16 h.

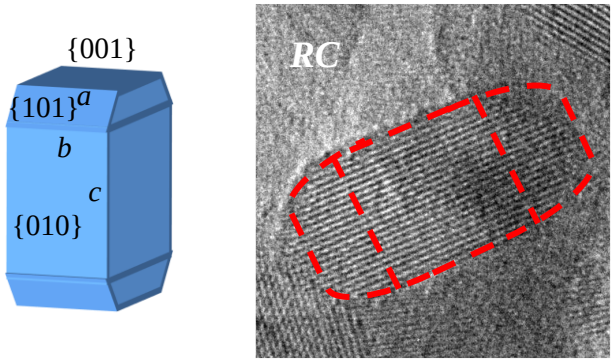

Figure 1. Geometrical model of nearly rectangular TiO_2 nanocrystals (*RC*) with {010}, {101} and {001} exposed surfaces.

Removal of capping agent residuals from the TiO_2 nanocrystals. In order to completely remove the residual amounts of capping agents strongly adsorbed on the titania surface, the dried TiO_2 nanocrystals were treated first with a superhydride solution (1 M lithium triethylborohydride in THF), which promote the reduction of OA, and then with a solution of dilute sulfuric acid to remove the excess of OM still coordinated to the surface.
This procedure was already shown to be efficient in cleaning without any morphology change.[18]

UV-Vis Diffuse Reflectance (UV-DRS). UV-DRS spectra of carefully ground naked nanocrystals powders were recorded in the range 800-200 nm with a by a UV Lambda 900 Perkin Elmer spectrophotometer, equipped with a diffuse reflectance accessory Praying–Mantis sampling kit (Harrick Scientific Products, USA). A Spectralon® disk was used as reference material.

Photocatalytic tests. The activity of the photocatalyst powders in hydrogen production by methanol photo-steam reforming $CH_3OH + H_2O \rightarrow CO_2 + 3\ H_2$ was tested in a closed recirculation laboratory scale apparatus described in previous studies.[32,33] Briefly the photocatalyst powder (14 mg) was mixed with distilled water (1.2 mL), deposited on 0.85–0.42 mm quartz beads (3 g) and dried at 70 °C for 2 h. The so obtained photocatalyst bed was inserted into the photoreactor consisting in a flat cylindrical Plexiglas cell, frontally closed by a Pyrex glass optical window (irradiation surface ca. 20 cm^2), which was connected to a closed stainless steel system. After preliminary thorough purging with nitrogen in order to remove any trace of

oxygen, the photocatalyst bed was continuously fed at 40 mL min^{-1} with a stream of N_2 saturated by the vapor of a 20 vol.% methanol–water solution (methanol molar fraction x = 0.10 in the liquid phase), kept at 30 °C.

The absolute pressure of the reactor, 1.2 bar at the beginning of the runs, slightly increased during irradiation, due to the accumulation of gas phase products. During the runs, typically lasting 6 h, the recirculating gas was automatically sampled on-line every 30 min and injected into an Agilent 6890 N gas-chromatograph, equipped with two columns, two detectors (thermoconductivity and flame ionization) and a Ni-catalyst kit for CO and CO_2 methanation. N_2 was used as carrier gas. The GC response was preliminarily calibrated for H_2, CO and CO_2 analysis. All kinetic tests were repeated two times.

The irradiation source, always switched on 30 min prior the beginning of the run and placed at 20 cm from the reactor, was a Xenon arc lamp (LSH302, LOT Oriel, 300 W), having 40.0 mW cm^{-2} irradiation intensity, and operative in the $350 < \lambda < 400$ nm range, as measured with an optical power meter (Thorlabs PM200) equipped with a thermal power sensor (Thorlabs S302C).

ESR investigation. The Electron Spin Resonance (ESR) investigation was performed by a Bruker EMX spectrometer operating at the X-band frequency and equipped with an Oxford cryostat. The nanocrystals were charged into quartz glass tubes connected both to a high vacuum pumping system and to a controlled gas feed, i.e. N_2 saturated with CH_3OH/H_2O vapors obtained by continuously bubbling the gas into a CH_3OH/H_2O 20 vol.% solution. Irradiation was performed by a UV-Vis 150 W Xe lamp (Oriel) on samples in the cavity through an optical fiber

(50 cm length, 0.3 cm diameter). Samples were irradiated at 130 K either in *vacuo* or in the presence of 10 mbar of O_2 or N_2 saturated with CH_3OH/H_2O. The spectra were recorded at the same temperature in *vacuo* (10^{-5} mbar) before, during and after 30 min-long irradiation, using a modulation frequency of 100 kHz, modulation amplitudes of 2-5 Gauss and a microwave power of 10 mW.

The *g* values were calculated by standardization with α,α′-diphenyl-β-picryl hydrazyl (DPPH). The spin concentration was obtained by double integration of the resonance lines, referring to the area of the standard Bruker weak pitch (9.7×10^{12} ± 5% spins cm^{-1}). Accuracy on double integration was ± 15%. Care was taken to always keep the most sensitive part of the ESR cavity (1 cm length) filled. Spectra simulations and fits were performed using the SIM 32 program.[34] For each sample, the absence of any signal before irradiation was checked.

RESULTS AND DISCUSSION

Morphological characterization. Figure 2 shows TEM and HRTEM images of differently shaped anatase nanoparticles. According to the results reported by Dihn et al.,[28] when the synthesis was carried out with a TB/OA/OM = 2:5:5 ratio at 180°C, almost rectangular TiO_2 nanocrystals (*RC*) with rather homogeneous shape and size (15 nm in length) were obtained (Fig. 2a, b and c). As observed in our previous study,[18] rhombic nanocrystals (*R*) very homogeneous in shape and size (13.5 nm in length) are obtainable (Fig. 2d, e and f) at the same reaction temperature with a TB/OA/OM = 1:4:6 ratio, while further increase of OA concentration

(TB/OA/OM = 1:8:2) and lower reaction temperature (140 °C) lead to the formation of the small nanobars (*NB*, 13 nm length) shown in Figure 2 (g, h and i).

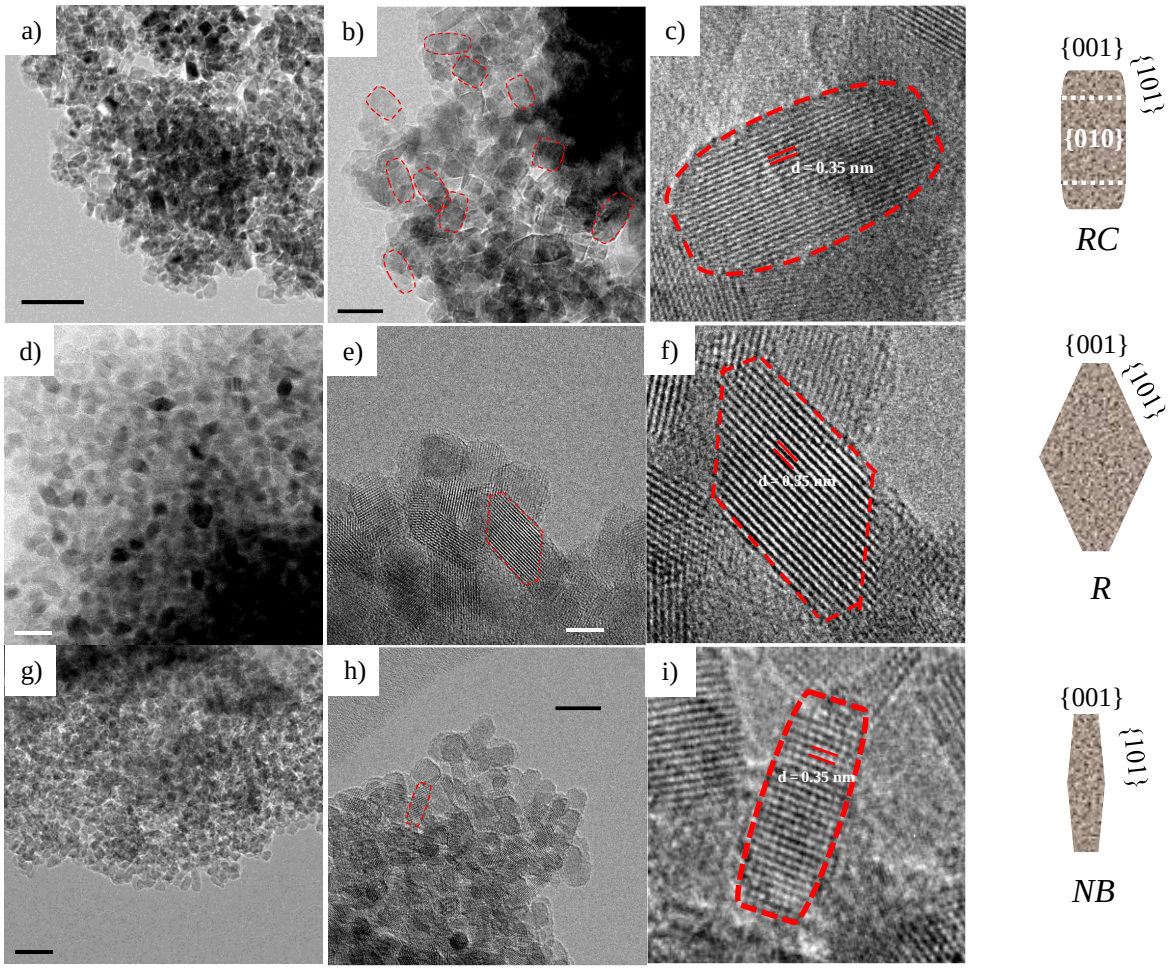

Figure 2. TEM and HRTEM images of shape-controlled TiO_2 nanocrystals produced by solvothermal synthesis. a), b) and c): Rectangular-shaped nanoparticles (*RC*); d), e) and f): rhombic nanocrystals (*R*); g), h) and i): nanobars (*NB*). The inset in the HRTEM images evidence the exposition of the {001}, {010} and {101} crystal surfaces. The 2D geometrical models of the nanocrystals and of their exposed surfaces are reported on the right.

Higher magnifications of *RC* and *R* lattice fringes along the [010] direction (Fig. 2c, f and i) clearly reveal the presence of (101) and (011) crystallographic planes with lattice space of 0.35 nm. This indicates that the crystal growth mainly occurs on the {001} face, which becomes less dominant moving from *RC* to *NB* nanocrystals. These information confirms that the nanoparticles mainly expose the {001} and {101} surfaces, respectively, with the additional presence of a significant amount of exposed {010} faces for *RC* nanocrystals.

The average *a*, *b*, and *c* values were calculated based on TEM and HRTEM analysis (see Figure 1). They correspond to the minimum and the maximum side of the {001} square face and to the longer side of the {010} rectangular face in *RC* particles (See Experimental Section). From these values and according to equation (1), the percentages of {001}, {101} and {010} exposed crystal faces for *RC* nanocrystals were determined and reported in Table 1, together with the percentages of {001} and {101} facets for *R* and *NB* nanocrystals taken from our previous study.[18]

Table 1. Morphological parameters of shape-controlled TiO_2 nanocrystals.

Sample	SSA_{BET} ($m^2\ g^{-1}$)	{001} faces (%)	{101} faces (%)	{010} faces (%)	SSA_{BET} of {001} faces ($m^2\ g^{-1}$)	SSA_{BET} of {101} faces ($m^2\ g^{-1}$)	SSA_{BET} of {010} faces ($m^2\ g^{-1}$)
RC	184	15.1	22.0	62.9	27.8	40.5	115.7
NB	227	5.8	94.2	0	13.2	213.8	0
R	199	10.6	89.4	0	21.1	177.9	0

Nitrogen physisorption experiments were performed on all shape-controlled TiO_2 nanocrystals after the removal of the capping agents. As already reported [18], *NB* and *R* samples are

mesoporous and exhibit a type IV Brunauer isotherm behavior (see details in Supporting Information). In the case of *RC* nanocrystals, analogous results have been obtained (Figure 3). According to the *t*-plot, no micropores were detected.

The specific surface areas (SSA_{BET}) of differently shaped TiO_2 nanocrystals are reported in Table 1. By considering the percentage of the mainly exposed {001}, {101} and {010} crystal faces, their relative SSA_{BET} were also calculated.

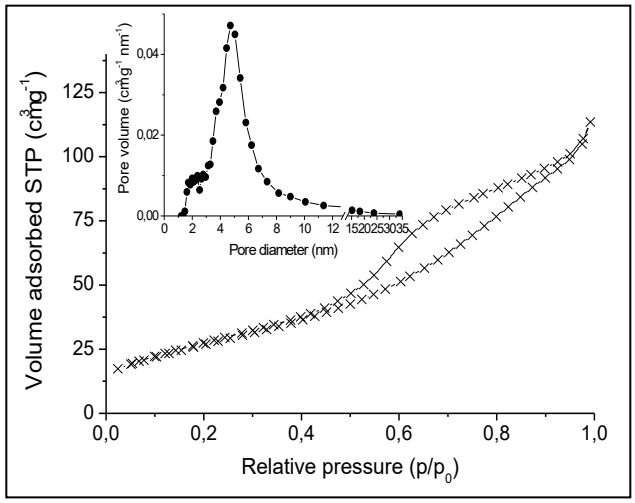

Figure 3. Adsorption/desorption isotherm at liquid nitrogen temperature for *RC* TiO_2 nanocrystals. The curve corresponds to a type IV isotherm with capillary condensation in the mesopores. Inset: pore size distribution.

Removal of capping agent residuals from the TiO_2 nanocrystals. The removal of capping molecules from the surface of morphology-controlled anatase nanoparticles, after washing with superhydride solution and dilute sulphuric acid solutions[18], was preliminary investigated by ATR-FTIR spectroscopy. In particular, Figure 4a shows the spectra of *NB* nanocrystals before (as-prepared) and after the cleaning procedure (clean *NB*). In *as-prepared NB* spectrum, the bands between 3000 and 3300 cm^{-1} can be interpreted as OH groups on the titania surface, originating from ethanol and water molecules involved in the experimental steps. The two sharp bands at 2845 and 2915 cm^{-1} are instead attributable to the symmetric and antisymmetric CH_2 stretching vibrations of OA and OM chains [19-20].

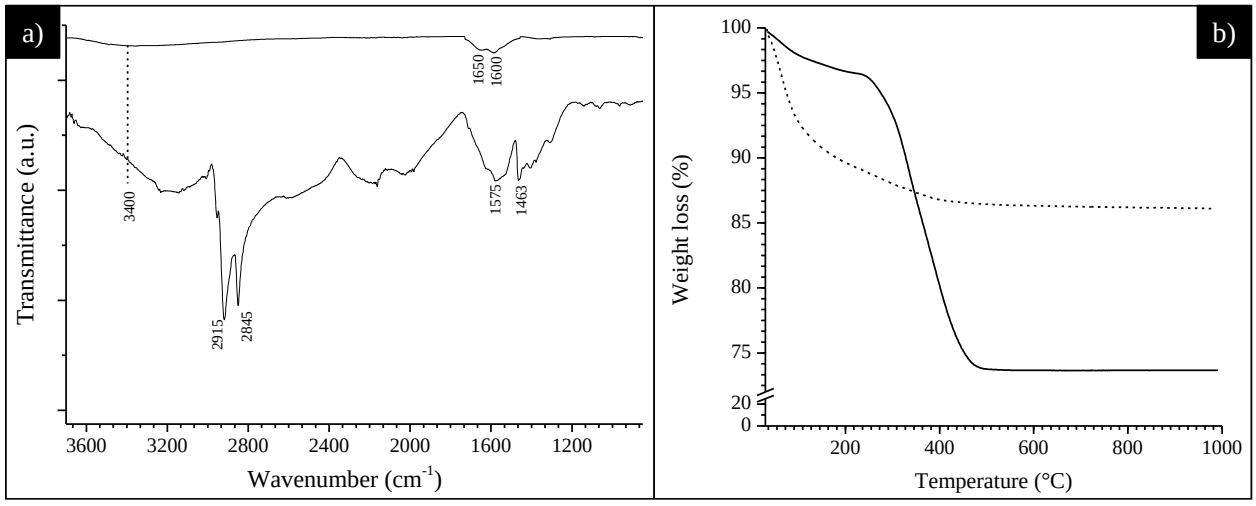

Figure 4. a) ATR-FTIR spectra of *NB* nanocrystals before (*as-prepared NB*) and after the cleaning procedure (*clean NB*); b) TGA curve of *NB* nanocrystals before (solid line, —) and after (dashed line, ----) the removal of the capping agents.

Weaker and broader bands at 1463 and 1575 cm^{-1} are also detectable, and can be assigned to the symmetric and antisymmetric stretching vibrations of the carboxylate groups of oleic acid with bidentate coordination mode on the TiO_2 surface [20]. These features superimpose to a broader band centered at 1625 cm^{-1} ascribed to water and/or hydroxyl species absorbed on the surface of the TiO_2 nanoparticles [19].

After the cleaning procedure, all the vibrations related to organic molecules disappear and the spectrum of *clean NB* nanocrystals shows exclusively broad bands at 3370 cm^{-1} and between 1650 and 1630 cm^{-1} corresponding to water and/or hydroxyl groups absorbed on the surface of the TiO_2 nanobars [19-20].

To further assess the removal of the organic capping agents, thermogravimetric analysis was performed on both as-prepared and naked nanocrystals. As representative example, Figure 4b reports the weight loss curves of the *NB* sample before (solid line) and after the washing treatment (dashed line). The as-prepared sample (solid line) shows an initial weight loss (~ 4%) beginning at nearly 33°C and continuing till 220°C attributable to physisorbed ethanol and water solvents. A second more evident weight loss occurs from 240 to 510°C, which can be associated to the thermal degradation of oleic acid and oleylamine units. Conversely, after the cleaning procedure, the nanobar-shaped nanocrystals display a single weight loss (~ 13 %) between 33 and 330°C, ascribed to the removal of the surface physisorbed cleaning solvents. These results support a fairly complete elimination of the organic capping agents after the washing treatment.

Similar ATR-FTIR and TGA results have been obtained for *R* and *RC* samples.

UV-Vis Diffuse Reflectance Spectroscopy (UV-DRS). The UV–DRS spectra of shape controlled TiO_2 nanocrystals are shown in Fig. S2 (Supporting Information). Diffuse reflectance data were converted into $F(R_\infty)$ values according to the Kubelka–Munk equation. All the samples show a band-gap value of ca. 3.2 eV, indicating that the different morphological features does not induce any substantial variation of the energy needed for band–band transition.

Photocatalytic tests: MeOH photosteam reforming. The trend of the hydrogen evolution during the photocatalytic steam reforming of methanol employing differently shaped TiO_2 catalysts are is reported in Figure 5. To support both the reliability and the reproducibility of the catalytic results, Table 2 summarizes the average H_2 evolution rates (r_{H_2}) and the relative standard deviations after three kinetic runs.

A performance dependence on the particle shape clearly results. In particular, the highest photoactivity occurs for the nearly rectangular-shaped particles (*RC*), though they display the lowest SSA_{BET} (see Table 1). Despite their relatively high specific surface area, the rhombic nanoparticles *R* and tiny *NBs* exhibit lower photoefficiency than *RCs*. These results indicate that the differences in particle size and total surface area of TiO_2 nanocrystals are not fully responsible for their photocatalytic properties, while suggesting that the exposed crystal faces and their relative specific surface area may account for their different performance.

Among the nanocrystals containing only {001} and {101} faces, the highest rate of H_2 production was attained by small *NBs*, which are characterized by the largest SSA_{BET} of {101} surfaces. This first result is in agreement with our previous study[18] where we suggested that the

{001} surfaces behave essentially as oxidation sites, while the {101} effectively provide reductive sites. The higher activity of {101} facets in H_2 production from methanol solutions under solar illumination was recently outlined also by Gordon et al.,[37] who modulated the percentage of {101} facets by an alternative time-consuming non-aqueous seeded growth method. Similar results, demonstrating the relatively higher reducing power of {101} facets, were obtained by Tachikawa et al.[38,39] who directly evaluated the photoredox activity of anatase TiO_2 crystal faces by *in-situ* fluorescence.

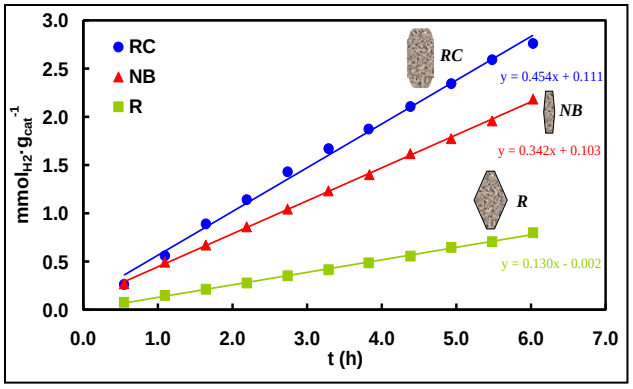

Figure 5. Hydrogen evolution during the photocatalytic steam reforming of methanol on shape controlled anatase nanocrystals.

Table 2. Mean zero-order rate constants of H_2 production on the investigated samples.

Sample	mean r_{H2} / mmol h^{-1} g^{-1}
RC	0.464 ± 0.003
NB	0.344 ± 0.003
R	0.136 ± 0.008

In the present case, according to Figure 5 and to the data reported in Table 2, the best photoefficiency in H_2 production was attained by the nearly rectangular *RC* nanocrystals, which display the highest specific surface area for exposed {001} facets, the lowest area for the {101} ones and also include the {010} faces. This beneficial effect on reactivity appears to be induced by the co-presence of {001}, {101}, and {010} facets, thus indicating the joint contribution of three different crystal facets in modifying the photoredox behavior.

It is worth highlighting that, in the present study, the enhancement of the photoefficiency induced by the coexistence of {001}, {101} and {010} surfaces has been obtained for shape-controlled TiO_2 nanocrystals grown through a fluorine-free wet-chemistry route. Therefore, any specific alteration of the electronic structure is avoided as well as the surface effects induced by residual surface fluorination[15, 21].

ESR investigation. ESR investigation provides information on the role of TiO_2 surfaces in increasing the electron and holes availability and in stabilizing the electron-hole separation. ESR spectra were recorded on shape-controlled TiO_2 nanocrystals, UV-Vis irradiated at 130 K directly in the ESR cavity, either *in vacuo* ($p < 10^{-5}$ mbar) or in the presence of 10 mbar of N_2 saturated with $MeOH/H_2O$ (20% v/v) vapors.

After irradiation under vacuum (Figure 6), all samples show two well separated sets of resonances. The lower field signals (Figure 6A) belong to different superimposed oxygen species,[18] namely hole traps (O^- species) and residual O_2^-,[40,41] whose *g* values are reported in Table 3.

As an example, the lower field resonances occurring in *RC* nanocrystals were resolved by simulation into three different components (Figure 6B): one orthorhombic species attributable to the superoxide centers (O_2^-) and two overlapping axial species attributable to holes trapped at two different O^- sites (O^- [I] and O^- [II], see Table 3). The presence of O_2^- species, mainly in *RC* nanocrystals, even when the UV-Vis irradiation was performed under vacuum, might be attributed to the reaction between residuals OH^- groups with photogenerated holes according to the mechanism proposed by Grätzel [42].

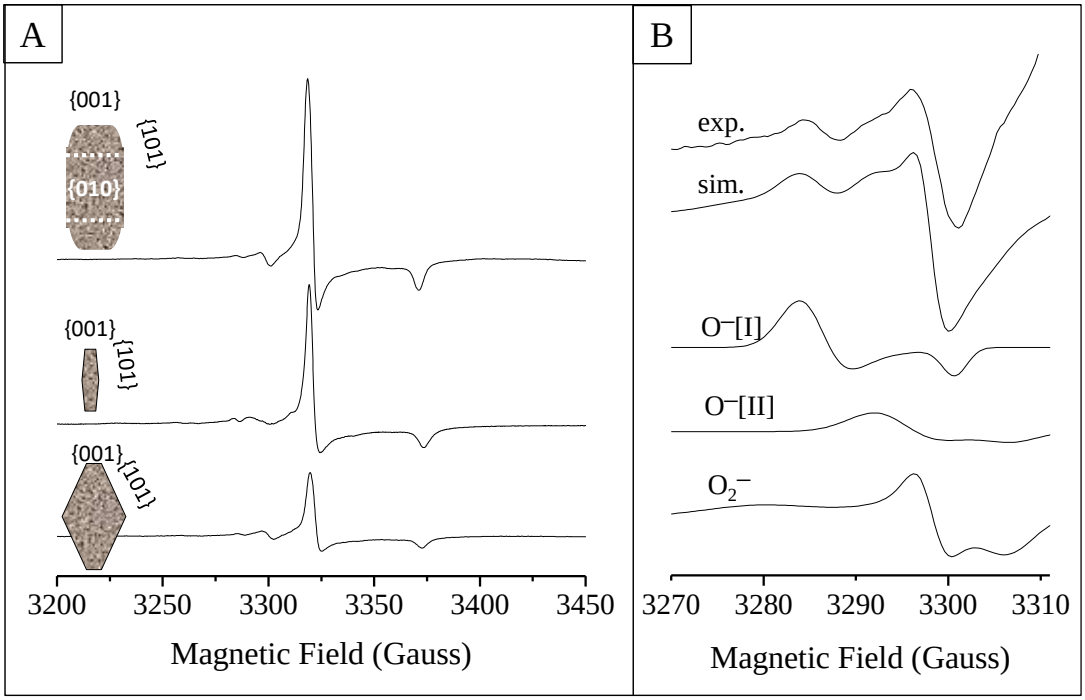

Figure 6. A) Experimental ESR spectra of differently shaped TiO_2 nanocrystals. Insets show the corresponding shapes. B) Magnification of the O^- spectral region for *RC* sample and deconvolution (simulation (sim)) of ESR signals (experimental (exp.)) into different O^- and O_2^- species.

The sharp higher field signals with axial symmetry and very similar *g* values (Figure 6A) are attributable to electrons trapped at Ti^{3+} centers.[43-46] Their intensity is much greater than that of other resonances and their sharpness suggests crystalline environment of the Ti^{3+} centers.

Table 3. *g* tensor values of the paramagnetic defects detected after photoexcitation in vacuum ($p < 10^{-5}$ mbar) in shape-controlled TiO_2 nanocrystals, determined by simulation of the ESR features. The relative contribution of the O^- species (calculated as percent of the $O^- + O_2^-$ signals total intensity) is reported as well as the amount of O^- and Ti^{3+} centers.

Sample	O^- centers (%)	O^- species	O_2^- species	Amount of O^- (spin g^{-1})	Ti^{3+} species	Amount of Ti^{3+} (spin g^{-1})
RC[b]	40	O^- [I]: $g_\perp$ = 2.0099, $g_\parallel$ = 2.0006 O^- [II]: $g_\perp$ = 2.0051, $g_\parallel$ = 1.9972	g_{zz} = 2.0145, g_{yy} = 2.0021, g_{xx}= 1.9994	1.49 x 10^{16}	$g_\perp$ = 1.9889 $g_\parallel$ = 1.9588	1.38 x 10^{18}
NB[a]	2	$g_\perp$ = 2.0126 $g_\parallel$ = 2.0046	O_2^-[I]: g_{zz} = 2.0252, g_{yy} = 2.0080, g_{xx}= 1.9990 O_2^-[II]: g_{zz} = 2.0212, g_{yy} = 2.0080, g_{xx}= 1.9990	4.16 x 10^{14}	$g_\perp$ = 1.9867 $g_\parallel$ = 1.9570	4.93 x 10^{17}
R[a]	78	O^- [I]: $g_\perp$ = 2.0090, $g_\parallel$ = 2.0001 O^- [II]: $g_\perp$ = 2.0050, $g_\parallel$ = 1.9975	O_2^-[I]: g_{zz} = 2.0254, g_{yy} = 2.0083, g_{xx}= 1.9990 O_2^-[II]: g_{zz} = 2.0215, g_{yy} = 2.0083, g_{xx}= 1.9990	6.01 x 10^{15}	$g_\perp$ = 1.9866 $g_\parallel$= 1.9575	3.54 x 10^{17}

[a] This study. [b]Taken from reference [18].

The relative contributions of the O^- species (calculated as percent of the $O^- + O_2^-$ signals total intensity) are summarized in Table 2. The amounts of O^- and Ti^{3+} centers, obtained by double integration of the spectral lines and referring the weak pitch area, are also reported.

It is well known that the UV-Vis irradiation of shape-controlled TiO_2 nanoparticles promotes the formation of different paramagnetic defects on different specific surfaces, causing variable photocatalytic performances.[17-22] In particular, in anatase nanocrystals with {001} and {101} exposed surfaces, we have recently found that the concentration of trapped holes (O^- centers) increases with the increase of the {001} surface area, while that of electron traps (Ti^{3+} centers) raises with the increase of the {101} ones.[18] These results suggested that {001} surfaces behave as primary oxidation sites playing a key role in the photoxidation reactions, while the {101} ones provide reductive sites and only indirectly contribute to the oxidative processes.

Accordingly, in the present case the concentration of trapped holes (O^- centers), calculated by double integration of the resonance lines, increases with the {001} surface area and becomes maximum for *RC* nanocrystals, with which the highest H_2 evolution rate was attained. This again points out the crucial role of the {001} surfaces in providing active sites for MeOH oxidation to CO_2.

For the nanocrystals containing only {001} and {101} faces, Ti^{3+} traps increase with increasing the specific surface area of {101} facets, and the small *NBs* which almost entirely expose such surfaces actually exhibit a higher amount of Ti^{3+} species compared to *R* nanocrystals (see Table 2). Surprisingly, the largest amount of Ti^{3+} occurs for the most reactive *RC* nanocrystals, characterized by the lowest percentage of {101} surfaces. This suggests that the additional exposition of the {010} faces in *RCs* has a role in inducing the high reactivity.[29]

In particular, we explain this behavior referring to the concept of "surface heterojunction" recently proposed by Jaroniec et al.[22] Based on DFT calculations, these authors reported that

{001} and {101} facets of anatase exhibit different band structures and band edge positions. In detail, the valence band (VB) of the {001} surfaces extends to higher energies in comparison to that of {101} ones, whereas the CB is located at a lower energy for {101} surfaces. Moreover, since {001} and {101} facets contact each other, their Fermi levels should be equal. The contiguous {001} and {101} facets can thus form a surface heterojunction within a single TiO_2 particle, promoting the selective migration of photogenerated electrons and holes toward the {101} and {001} facets, respectively. In our case, since {101} and {010} surfaces have very close band-gaps,[29] a similar mechanism involving adjacent {001}, {101} and {010} surfaces can be suggested for *RC* nanocrystals, where the electrons transfer from {001} facets is not just limited to the {101} but also proceeds effectively toward the {010} ones.

This increases the lifetime of the charge carriers, and explains the higher photoefficiency attained with the multi-faceted *RCs* compared to that of *NB* and *R* samples.

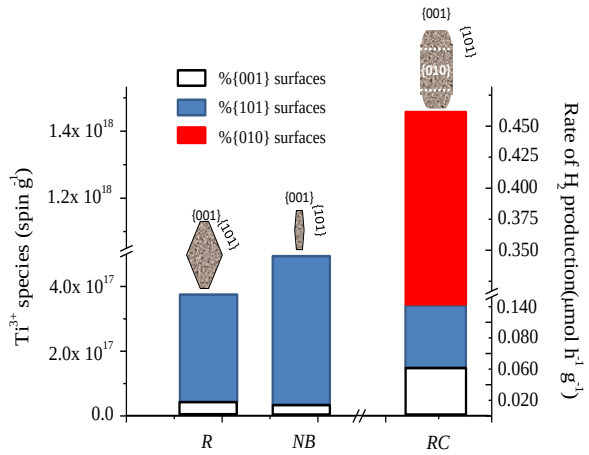

Figure 7. Relative abundance of Ti^{3+} species and measured H_2 evolution rate with *RC*, *NB* and *R* TiO_2 nanocrystals as a function of the relative percentage of exposed faces.

The above outcomes are summarized in Fig. 7, which compares the abundance of Ti^{3+} traps with the rate of H_2 production, for different relative percentages of {001}, {101} and {010} surfaces exposed by anatase nanocrystals. Both the amount of Ti^{3+} centers and the rate of H_2 evolution increase as the {101} fraction increases, but the maximum r_{H2} is obtained for the *RC* sample, containing a high percentage of {010} surfaces in conjunction with the highest percentage of {001} faces. This highlights that the presence of {010} faces further stabilizes the Ti^{3+} centers which, besides that provided by the {101} faces, can be potentially employed in the photoreduction reaction.

In order to better understand both the involvement of {101} and {010} surfaces and the role played by Ti^{3+} species in the H_2 production, the ESR investigation on *RC*, *NB* and *R* samples was performed after UV-Vis irradiation at 130 K in the presence of 10 mbar of N_2 saturated with MeOH/H_2O (20% v/v) vapors, thus simulating the condition experienced by the TiO_2 samples during the photocatalytic tests.

The complex signals at low magnetic field may be attributed to the superimposition of different species, mainly belonging to holes trapped in O^- species or generating O_2^- centers (Figure 7A). The presence of hydroxy-methyl radicals (•CH_2OH) produced by methanol photo-oxidation at the TiO_2 surface cannot be excluded, even if their detection is difficult at T > 77 K.[47, 48] At higher magnetic field, the intensity of the Ti^{3+} features becomes much lower than that detected in vacuum for all samples (Fig. 8A). In detail, the depletion of the electron trap species is more pronounced for *RC* than for *NB* and *R* nanocrystals (Fig. 8B).

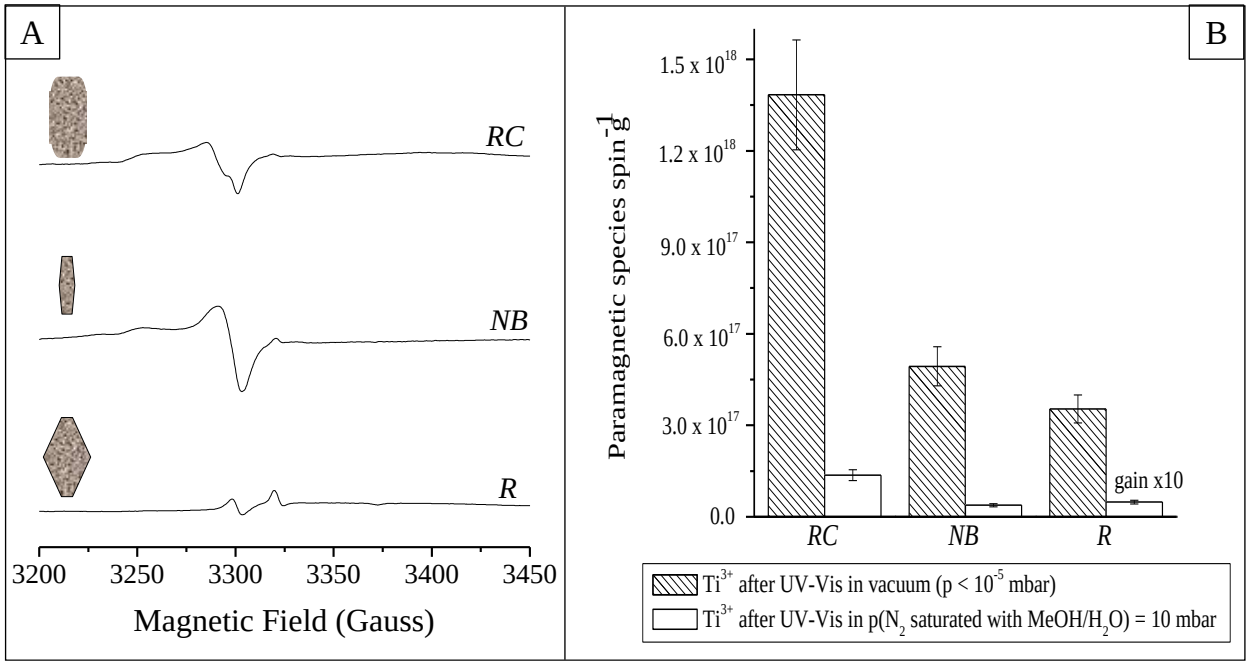

Figure 8. A) ESR spectra of shape-controlled anatase nanoparticles at 130 K after UV-Vis irradiation at 130 K in the presence of 10 mbar of N_2 saturated with MeOH/H_2O (20% v/v) vapors and subsequent evacuation at $p < 10^{-5}$ mbar. B) Amounts of Ti^{3+} species detected after UV-Vis irradiation either in vacuum ($p < 10^{-5}$ mbar) or in the presence of 10 mbar of N_2 saturated with MeOH/H_2O (20% v/v) for differently shaped nanocrystals.

Since H_2 evolution is associated with electron transfer, these results on one hand provide evidence of the significant involvement of the Ti^{3+} species in the reaction, on the other hand suggest that photoproduced electrons in anatase nanoparticles with highly exposed {010} and {101} may not only be efficiently entrapped as Ti^{3+} species (see Figure 7), but they can also be easily transferred to H^+ species to produce H_2.

CONCLUSIONS

The ESR investigation of the photogenerated defects in shape controlled anatase nanocrystals with {001}, {101} and {010} exposed surfaces, allows to understand the role of these crystal faces in tuning the hydrogen production in methanol photo steam reforming.

In particular, we found that the amount of the electrons traps (Ti^{3+}centers) parallels the rate of H_2 evolution and becomes maximum for the most reactive *RC* nanocrystals with the highest area of {001} surfaces and the lowest of {101}, but additionally containing a significant percentage of {010} faces. This indicates that the H_2 production not only to the envisaged reducing {101} facets, but also to the {010} ones.

More in depth, we suggest that the contiguous {001}, {101} and {010} facets can form an highly effective "surface heterojunctions" within a single *RC* particle, which allows the selective migration of the photogenerated electrons not just toward the {101} surfaces but also to the {010} ones, and of holes toward the {001}. This transfer increases the lifetime of the charge carriers, thus enhancing the photoefficiency of *RC*s compared to that of *NB* and *R* samples. Coherently, the highest concentration of holes traps (O^- centers) was detected for these nanocrystals, displaying the highest amount of oxidizing {001} surfaces.

UV photoexcitation in MeOH atmosphere leads to a partial annihilation of the Ti^{3+} features, mainly for highly reactive *RC* nanocrystals. Since the H_2 production needs an electron transfer, these outcomes probe the relevant contribution of the Ti^{3+} supplied by exposed {010} and {101} surfaces to the H^+ photoreduction reaction.

These outcomes and the adopted approach underline the importance of tuning the photogenerated defects by crystal facet engineering, in order to critically understand and further optimize the photocatalytic properties of nanocrystals.

AUTHOR INFORMATION

Corresponding Authors

*e-mail: massimiliano.darienzo1@unimib.it

mariavittoria.dozzi@unimi.it

ACKNOWLEDGEMENTS

This work has been performed in the frame of the European COST action MP1202 “Rational design of hybrid organic inorganic interfaces: the next step towards advanced functional materials”. MR thanks Corimav for its support within the PCAM European Doctoral Programme.

SUPPORTING INFORMATION

Additional figures concerning on N_2 physisorption of *NB* nanocrystals and UV-Vis Diffuse Reflectance (UV-DRS) spectra of shape controlled anatase nanoparticles are included. This material is available free of charge via the Internet at http://pubs.acs.org.

REFERENCES

(1) Turner, J.A. A Realizable Renewable Energy Future, *Science* **1999**, *285*, 687–689.

(2) Chen, X.; Shen, S.; Guo; L.; Mao, S.S. Semiconductor-Based Photocatalytic Hydrogen Generation, *Chem. Rev*., **2010**, *110*, 6503–6570.

(3) Maeda, K.; Domen, K. Photocatalytic Water Splitting: Recent Progress and Future Challenges, *J. Phys. Chem. Lett*., **2010**, *1*, 2655–2661.

(4) Osterloh, F.E. Inorganic Nanostructures for Photoelectrochemical and Photocatalytic Water Splitting, *Chem. Soc. Rev.*, **2013**, 42, 2294–2320.

(5) Zhang, K.; Liu, Q.; Wang, H.; Zhang, R.; Wu, C.; Gong, J.R. TiO_2 Single Crystal with Four-Truncated-Bipyramid Morphology as an Efficient Photocatalyst for Hydrogen Production, *Small* **2013**, *9*, 2452–2459.

(6) Wang, J.; Gao, M.; Ho, G.W. Bidentate-Complex-Derived TiO_2/Carbon Dot Photocatalysts: In Situ Synthesis, Versatile Heterostructures, and Enhanced H_2 Evolution, *J. Mater. Chem. A*, **2014**, *2*, 5703–5709.

(7) Ma, Y.; Wang, X.; Jia, Y.; Chen, X.; Han, H.; Li, C. Titanium Dioxide-Based Nanomaterials for Photocatalytic Fuel Generations, *Chem. Rev*. **2014**, *114*, 9987−10043.

(8) Liu, G.; Yang, H.G., Pan, J.; Yang, Y.Q.; Lu, G.C.; Cheng, H. M. Titanium Dioxide Crystals with Tailored Facets, *Chem. Rev.* **2014**, *114*, 9559−9612.

(9) Xu, H.; Ouyang, S.; Liu, L.; Reunchan, P.; Umezawa, N.; Ye, J. Recent Advances in TiO_2-Based Photocatalysis, *J. Mater. Chem. A*, **2014**, *2*, 12642-12661.

(10) Moniz, S.; Shevlin, S.; Martin, A.D.; Guo, Z; Tang, J. Visible-Light Driven Heterojunction Photocatalysts for Water Splitting – a critical review, *Energy Environ. Sci.*, **2015**, *8*, 731–759.

(11) Kandiel, T.A.; Anjum, D.H.; Takanabe K. Nano-Sized Quaternary $CuGa_2In_3S_8$ as an Efficient Photocatalyst for Solar Hydrogen Production, *ChemSusChem*, **2014**, *7*, 3112–3121.

(12) Ran, J.; Zhang, J.; Yu, J.; Jaroniec, M.; Qiao, S.Z. Earth-Abundant Cocatalysts for Semiconductor-Based Photocatalytic Water Splitting, *Chem. Soc. Rev.* **2014**, 43, 7787–7812.

(13) Naldoni, A.; D'Arienzo, M.; Altomare, M.; Marelli, M.; Scotti, R.; Morazzoni, F.; Selli, E.; Dal Santo, V. Pt and Au@TiO_2 Photocatalysts for Methanol Reforming: Role of Metal Nanoparticles in Tuning Charge Trapping Properties and Photoefficiency, *Appl. Catal., B* **2013**, *130*, 239–248.

(14) Dozzi, M.V.; Saccomanni, A.; Altomare, M.; Selli, E. Photocatalytic Activity of NH_4F-Doped TiO_2 Modified by Noble Metal Nanoparticle Deposition, *Photochem. Photobiol. Sci.* **2013**, *12*, 595–601.

(15) Dozzi M.V.; Selli, E. Doping TiO_2 with p-Block Elements: Effects on Photocatalytic Activity, *J. Photochem. Photobiol C: Photochem. Rev.* **2013**, 14, 13–28.

(16) Ong, W. J.; Tan, L., L.; Chai, S.P.; Yong, S.T.; Yu, S.; Mohamed, A.R. Facet-Dependent Photocatalytic Properties of TiO_2-Based Composites for Energy Conversion and Environmental Remediation, *ChemSusChem* **2014**, *7*, 690–719.

(17) Cargnello, M.; Diroll, T.B. Tailoring Photocatalytic Nanostructures for Sustainable Hydrogen Production, *Nanoscale* **2014**, *6*, 97–105.

(18) D'Arienzo, M.D.; Carbajo, J.; Bahamonde, A.; Crippa, M.; Polizzi, S.; Scotti, R.; Wahba, L.; Morazzoni, F. Photogenerated Defects in Shape-Controlled TiO_2 Anatase Nanocrystals: a Probe to Evaluate the Role of Crystal Facets in Photocatalytic Processes, *J. Am. Chem. Soc.* **2011**, *133*, 17652–1766.

(19) Gonzalo-Juan, I.; McBride, J. R. and Dickerson, James H. Ligand-Mediated Shape Control in the Solvothermal Synthesis of Titanium Dioxide Nanospheres, Nanorods and Nanowires, *Nanoscale*, **2011**, *3*, 3799–3804.

(20) Joo, J.; Kwon, S.G.; Yu, T.; Cho, M.; Lee, J.; Yoon, J. and Hyeon, T. Large-Scale Synthesis of TiO_2 Nanorods via Nonhydrolytic Sol−Gel Ester Elimination Reaction and Their Application to Photocatalytic Inactivation of E. coli, *J. Phys. Chem. B* **2005**, *109*, 15297–15302.

(21) Dozzi M.V.; Selli, E. Specific Facets–Dominated Anatase TiO_2: Fluorine-Mediated Synthesis and Photoactivity, *Catalysts* **2013**, 3, 455–485.

(22) Yu, J. G.; Low, J. X.; Xiao, W.; Zhou, P.; Jaroniec, M. Enhanced Photocatalytic CO_2-Reduction Activity of Anatase TiO_2 by Coexposed {001} and {101} Facets, *J. Am. Chem. Soc.* **2014**, *136*,8839–8842.

(23) Selloni, A. Crystal growth: Anatase Shows its Reactive Side, *Nat. Mater*. **2008**, *7*, 613–615.

(24) Liu, S.W.; Yu, J.G.; Jaroniec, M. Tunable Photocatalytic Selectivity of Hollow TiO_2 Microspheres Composed of Anatase Polyhedra with Exposed {001} Facets, *J. Am. Chem. Soc.* **2010**, *132*, 11914–11916.

(25) Zhang, D.; Li, G.; Yang, X.; Yu, J.C. A Micrometer-Size TiO_2 Single–Crystal Photocatalyst with Remarkable 80% Level of Reactive Facets, *Chem. Comm*. **2009**, *29*, 4381–4383.

(26) Han, X.; Kuang, Q.; Jin, M.; Xie Z.; Zheng, L. Synthesis of Titania Nanosheets with a High Percentage of Exposed (001) Facets and Related Photocatalytic Properties, *J. Am. Chem. Soc.* **2009**, *131*, 3152–3153.

(27) Zhu, J.; Wang, S.; Bian, Z.; Xie, S.; Cai, C.; Wang, J.; Yang, H.; Li, H. Solvothermally Controllable Synthesis of Anatase TiO_2 Nanocrystals with Dominant {001} Facets and Enhanced Photocatalytic Activity, *Cryst. Eng. Comm*. **2010**, *12*, 2219–2224.

(28) Yang, X.H.; Li, Z.; Liu, G.; Xing, J.; Sun, C.; Yang, H.G.; Li, C. Ultra-thin Anatase TiO_2 Nanosheets Dominated with {001} Facets: Thickness–Controlled Synthesis, Growth Mechanism and Water–Splitting Properties, *Cryst. Eng. Comm*. **2011**, *13*, 1378–1383.

(29) Pan, J.; Liu, G.; Lu, G.Q.; Cheng, H.M. On the True Photoreactivity Order of {001}, {010}, and {101} Facets of Anatase TiO_2 Crystals, *Angew. Chem. Int. Ed.* **2011**, *50*, 2133–2137.

(30) Dinh, C.T.; Nguyen, T.D.; Kleitz, F.; Do T.O. Shape-Controlled Synthesis of Highly Crystalline Titania Nanocrystals, *ACS Nano* **2009**, *3*, 3737–3743.

(31) Xiang, Q.; Yu, J.; Jaroniec M. Tunable Photocatalytic Selectivity of TiO_2 Films Consisted of Flower-Like Microspheres with Exposed {001} Facets, *Chem. Comm*. **2011**, *47*, 4532–4534.

(32) Brunauer, S.; Emmet, P.H.; Teller, E. Adsorption of Gases in Multimolecular Layers, *J. Am. Chem. Soc*. **1938**, *60*, 309–319.

(33) Barret, E.P.; Joyner, L.G.; Halenda, P.P. The Determination of Pore Volume and Area Distributions in Porous Substances. I. Computations from Nitrogen Isotherms, *J. Am. Chem. Soc.* **1951**, 73, 373–380.

(34) Chiarello, G.L.; Aguirre M.H.; Selli, E. Hydrogen Production by Photocatalytic Steam Reforming of Methanol on Noble Metal–Modified TiO_2, *J. Catal.* **2010**, *273*, 182–190.

(35) Chiarello, G.L.; Forni L.; Selli, E. Photocatalytic Hydrogen Production by Liquid– and Gas–Phase Reforming of CH_3OH over Flame-Made TiO_2 and Au/TiO_2, *Catal. Today*, **2009**, *144*, 69–74.

(36) Adamski, A.; Spalek, T.; Sojka, Z. Application of EPR Spectroscopy for Elucidation of Vanadium Speciation in VO_x/ZrO_2 Catalysts Subject to Redox Treatment, *Res. Chem. Intermed*. **2003**, *29*, 793–804.

(37) Gordon, T.R.; Cargnello, M.; Paik, T.; Mangolini, F.; Weber, R.T.; Fornasiero, P.; Murray, C.B. Nonaqueous Synthesis of TiO_2 Nanocrystals Using TiF_4 to Engineer Morphology, Oxygen Vacancy Concentration, and Photocatalytic Activity**,** *J. Am. Chem. Soc.* **2012**, *134*, 6751–6761.

(38) Tachikawa, T.; Wang, N.; Yamashita, S.; Cui, S.C.; Majima, T. Design of a Highly Sensitive Fluorescent Probe for Interfacial Electron Transfer on a TiO_2 Surface, *Angew. Chem. Int. Ed.* **2010**, *49*, 8593–8597.

(39) Tachikawa, T.; Majima, T. Single-Molecule, Single-Particle Fluorescence Imaging of TiO_2-Based Photocatalytic Reactions, *Chem. Soc. Rev.* **2010**, *39*, 4802–4819.

(40) Berger, T.; Diwald, O.; Knozinger, E.; Sterrer, M.; Yates, J. T. UV Induced Local Heating Effects in TiO_2 Nanocrystals, *Phys. Chem. Chem. Phys.* **2006**, *8*, 1822–1826.

(41) Carter, E.; Carley, A. F.; Murphy, D. M. Evidence for O_2^- Radical Stabilization at Surface Oxygen Vacancies on Polycrystalline TiO_2, *J. Phys. Chem. C* **2007**, *111*, 10630–10638.

(42) Howe, R.F.; Gratzel, M. EPR Study of Hydrated Anatase under UV Irradiation, *J. Phys. Chem.* **1987**, *91*, 3906–3909.

(43) Hurum, D.C.; Agrios, A.G.; Gray, K.A.; Rajh, T.; Thurnauer, M.C. Explaining the Enhanced Photocatalytic Activity of Degussa P25 Mixed-Phase TiO_2 Using EPR, *J. Phys. Chem. B* **2003**, *107*, 4545–4549.

(44) Berger, T.; Sterrer, M.; Diwald, O.; Knozinger, E.; Panayotov, D.; Thompson, T.L.; Yates, J.T. Light-Induced Charge Separation in Anatase TiO_2 Particles**,** *J. Phys. Chem. B* **2005**, *109*, 6061–6068.

(45) Scotti, R.; D'Arienzo, M.; Testino, A.; Morazzoni, F. Photocatalytic Mineralization of Phenol Catalyzed by Pure and Mixed Phase Hydrothermal Titanium Dioxide, *Appl. Catal., B* **2009**, *88*, 497–504.

(46) Scotti, R.; Bellobono, I.R.; Canevali, C.; Cannas, C.; Catti, M.; D'Arienzo, M.; Musinu, A.; Polizzi, S.; Sommariva, M.; Morazzoni, F. et al. Sol-Gel Pure and Mixed-Phase Titanium Dioxide for Photocatalytic Purposes: Relations between Phase Composition, Catalytic Activity, and Charge-Trapped Sites, *Chem. Mater.* **2008**, *20*, 4051–4061.

(47) Micic, O.I.; Zhang, Y.; Cromack, K.R.; Trifunac, A.D.; Thurnauer, M.C. Photoinduced Hole Transfer from Titanium Dioxide to Methanol Molecules in Aqueous Solution Studied by Electron Paramagnetic Resonance, *J. Phys. Chem.* **1993**, *97*, 13284–13288.

(48) Shkrob, I.A.; Marin, T.W.; He, H.; Zapol, P. Heteroatom-Transfer Coupled Photoreduction and Carbon Dioxide Fixation on Metal Oxides, *J. Phys. Chem. C* **2012**, *116*, 9450–9460.

SYNOPSIS (TOC)